

Numerical Heat Transfer, Part A: Applications

An International Journal of Computation and Methodology

ISSN: (Print) (Online) Journal homepage: www.tandfonline.com/journals/unht20

An empirical analysis of hybrid MHD ferrofluid unsteady flow of two-dimensional heat transfer across a porous channel

Qadeer Raza, Rabia Younus, Hassan Ali Ghazwani & Ali J. Chamkha

To cite this article: Qadeer Raza, Rabia Younus, Hassan Ali Ghazwani & Ali J. Chamkha (29 Jul 2024): An empirical analysis of hybrid MHD ferrofluid unsteady flow of two-dimensional heat transfer across a porous channel, Numerical Heat Transfer, Part A: Applications, DOI: [10.1080/10407782.2024.2382911](https://doi.org/10.1080/10407782.2024.2382911)

To link to this article: <https://doi.org/10.1080/10407782.2024.2382911>



Published online: 29 Jul 2024.



Submit your article to this journal [↗](#)





View related articles [↗](#)



View Crossmark data [↗](#)



An empirical analysis of hybrid MHD ferrofluid unsteady flow of two-dimensional heat transfer across a porous channel

Qadeer Raza^a , Rabia Younus^b, Hassan Ali Ghazwani^c, and Ali J. Chamkha^d 

^aSchool of Mathematics and Statistics, Xi'an Key Laboratory of Scientific Computation and Applied Statistics, Northwestern Polytechnical University, P.R. China; ^bDepartment of Mathematics, AIR University, Multan Campus, Multan, Pakistan; ^cDepartment of Mechanical Engineering, College of Engineering and Computer Science, Jazan University, Saudi Arabia; ^dFaculty of Engineering, Kuwait College of Science and Technology, Kuwait City, Kuwait

ABSTRACT

This research investigates the heat transfer dynamics of a two-dimensional, incompressible, laminar, magnetohydrodynamics, time-dependent flow of a hybrid ferromagnetic fluid with radiation and irregular heat source/sink conditions through two porous channels. The study investigates the unique capability of ferromagnetic solid nanoparticles to improve the thermal efficiency of the host fluid, with potential applications in medicine such as drug targeting, cell separation, and magnetic resonance imaging. A mathematical model is developed as a nonlinear partial differential equation (PDE), which is subsequently converted into a nonlinear ordinary differential equation (ODE) using similarity transformations. The numerical solution is obtained using the 4th-order Runge-Kutta method implemented in Mathematica software. We analyze the impact of various nondimensional factors on the numerical results, including skin friction coefficient and Nusselt number, as well as graphical results depicting the velocity and temperature profiles of the hybrid ferrofluid. Boosting the film thickness parameter (λ) improves the heat transfer rate at the bottom of the porous channel. Raising the irregular heat source/sink parameters (A^* and B^*) and causing opposite impacts on the heat transfer rate at the bottom porous channel. Higher the radiation (R) values, the temperature profile behaves oppositely in both porous channels. The analysis reveals that the hybrid ferrofluid exhibits a higher rate of heat transfer compared to the ferrofluid.

ARTICLE HISTORY

Received 16 May 2024
Revised 8 July 2024
Accepted 15 July 2024

KEYWORDS

Heat transfer; hybrid ferrofluid; magnetohydrodynamics; irregular heat source/sink; porous channel; thermal radiation

1. Introduction

Ferrofluids, such as exhibit strong magnetization when exposed to magnetic fields. Developed in 1963 by NASA's Steve Papal for liquid rocket fuel, they can be drawn into pump inlets with zero friction. Consisting of base fluids and magnetic nanoparticles, recent advancements include permanent magnetic ferrofluids resistant to external fields. Used for vibration damping, they find applications in computer hard drives, engines, and medical imaging contrast agents. Despite their attraction to ions in the presence of magnets, ferrofluids respond to outward magnetic fields, enabling position monitoring. Their molecules remain stable under magnetic fields, preventing dispersion over time. Preservative treatment prevents clumping, maintaining stability and predictable behavior. The fluid's structure gives it solid-like properties, altering viscosity rapidly under magnetic fields. In biological contexts, ferrofluids act as biomagnetic fluids, as seen in blood

CONTACT Qadeer Raza  qadeerraza@mail.nwpu.cn  School of Mathematics and Statistics, Xi'an Key Laboratory of Scientific Computation and Applied Statistics, Northwestern Polytechnical University, 710129, P.R. China.

Nomenclature

u, v	x and y component of the velocity (m/s)	K^*	mean absorption coefficient
μ_f	base fluid dynamic viscosity kg/(m·s)	K_f	base fluid thermal conductivity (W/(m·K)).
T	temperature of the fluid (K)	k_s	ferro particle thermal conductivity (W/(m·K))
ϕ_1 and ϕ_2	ferro particles 1 st and 2 nd volume fraction	σ^*	Stefan-Boltzmann constant
F	dimensionless stream function	bf	base Fluid
θ	dimensionless temperature profile	F_{fd}	ferrofluid
ρ_{hffd}	density hybrid ferrofluid (kg/m ³)	A^* or B^*	correspond to nonuniform heat/sink source
Pr	Prandtl number	λ	film thickness parameter
q''	nonuniform heat source/sink	R	radiation parameter
M	magnetic field parameter	HF_{fd}	hybrid ferrofluid
Re	Reynolds number		
μ_{hffd}	hybrid ferrofluid dynamic viscosity kg/(m·s)		

containing iron oxide hemoglobin. This property classifies blood as a ferromagnetic or paramagnetic gas. Ferrofluid ferro-hydrodynamics differs significantly from magnetic forces, emphasizing their unique behavior. Many researchers have worked in the field of ferrofluids. Hayat *et al.*, [1] studied chemical reactions in 2D ferrofluid flows with magnetic dipoles and mixed convection caused by sheet stretching. In their study, Zeeshan *et al.*, [2] scrutinized that ferrofluids react to magnetic fields and how radioactive compounds are transported through them. Ferrofluids are liquid mixtures containing iron nanoparticles and surfactants. Sadrhosseini *et al.*, [3] investigate the improvement of heat transfer in a tube containing permeable material subjected to a uniform wall heat flux and magnetic field. They discovered that the proportion of ferrofluid volume has a significant impact on heat transfer. Khalid *et al.*, [4] explore the impact of magnetohydrodynamics (MHD) and porosity on a ferrofluid flowing across a vibrating plate with varying wall temperatures. They use cylindrical nanoparticles suspended in kerosene oil as the base fluid. Abbas *et al.*, [5] explore ferrofluid flow across an expanding sheet in a porous medium, focusing on the effect of the magnetic dipole on fluid dynamics. The effect of magnetic fields on the flow of ferrofluid in a porosity tube is studied by Sehat *et al.*, [6]. In this study, Saeed *et al.*, [7] study the ferrofluid's continuous movement in a thin media that responds to changes in temperature. Borglin *et al.*, [8] investigate the effects of magnetic fields on ferrofluid behavior in porous media and speculate on the implications for flow regulation.

Heat transfer is an important implement for controlling temperatures in many different types of businesses, and there are several ways to make it even more efficient. Because of their superior thermal transport qualities, nanofluids show great promise for enhancing the heat transfer properties of base fluids. Colloidal suspensions of magnetic particles in a base fluid are called ferrofluids. To keep the particles from sticking together because of van der Waals interactions, these fluids include surfactants. As nanofluids, ferrofluids with magnetic features outperform more traditional fluids, such as water and ethylene glycol, in terms of heat conductivity. Additionally, they can increase heat transfer rates by manipulating the boundary layer thickness in a magnetic field. Ilias *et al.*, [9] investigate the constant convection that occurs in the boundary layer flow of MHD ferrofluids over a vertical flat plate by measuring thermal transfer parameters and patterns of motion. Usman *et al.*, [10] investigate the MHD boundary-layer flow of ferrofluids across a flat plate for heat transfer research. Sheikhejad *et al.*, [11] investigated the magnetic field's effect on the assisted convective of ferrofluid in a partly filled porous tube, which improved heat transmission. By studying the effects of a perpendicular magnetic field on the distribution of

temperatures and thermal boundary conditions, Ghosh *et al.*, [12] showed that ferrofluids can undergo heat transfer while flowing over a parallel plate channel. Nessab *et al.*, [13] analyzed energy transfer and ferrofluid movement in a channel with staggered magnetic sources and observed that a higher magnetic number and a lower inlet height resulted in improved heat exchange. Saleem *et al.*, [14] studied radiative heat flux and magnetized Casson nanofluid flow on a nonlinear stretching surface, employing Brownian motion and thermophoresis processes. Ahmad *et al.*, [15] analyzed the thermal impacts of micropolar nanofluids, finding that material characteristics reduced velocity profiles while porosity parameters increased concentrations. Saleem *et al.*, [16] evaluated the MHD incompressible flow of hybrid nanoparticle-colloidal combinations with base fluid, specifically the effects of thermal radiation and viscous dissipation on temperature profiles. To investigate the impacts of magnetohydrodynamics on heat and mass transmission, Raza *et al.*, [17] investigated six different types of nanoparticles in hybrid nanofluids over porous surfaces. Khalil *et al.*, [18] explored fluid dynamics involving hybrid nanoparticles on an elastic surface. They unveiled enhanced heat conductivity and intricate interactions shaping thermal transport within porous materials. Raza *et al.*, [19] developed a mathematical model to investigate the effects of porous surfaces on energy and mass transfer processes in nanofluid flow, revealing increases in thermal conductivity and performance.

Ferrofluids are a fairly complex solid suspension of superparamagnetic single-domain particles in a carrier fluid [20, 21]. Through the application of a magnetic field to a ferrofluid, a particle moves to a place with the largest amount of magnetic flux. Such property enables the ferrofluid to be restricted, for example, to a ring form and thereby create a barrier. The liquid design of such seal rings helps them adapt their form to the piston and seal house output errors. This change of form does not cause seal leakage or friction. Positive properties, such as seal regeneration, have been found during pressure release. For revolving shafts, identical ferrofluid seals have already been proposed [22, 23]. Choi *et al.*, [24] provided a numerical scheme using the revisited Kelvin force method for obtaining shape formation. The formula takes from the concept of the original Kelvin as well as the digital whole system's newly appreciated field intensity. Electromagnetic and gravitational body powers will be known for the hydrostatic equilibrium that is linked to the static magnetic field effect. Ferrofluid could be a free surface profile determined *via* computational simulations, relying on the assumption that the free surface pressures will remain the same. When multiple magnetic nanoparticles disperse in a conventional fluid, they form a hybrid nanofluid, which finds applications in damping, dynamic sealing, and heat dissipation [25, 26]. Applying a magnetic field to a ferrofluid causes particles to move toward areas with the highest magnetic flux, enabling the ferrofluid to be shaped into a ring form, creating an effective barrier. The liquid design of these seal rings allows them to adapt to piston and seal line output errors without causing leakage or friction. Positive properties, including seal regeneration during pressure release, have been observed. Similar ferrofluid seals have been proposed for revolving shafts [27, 28]. The study presents a novel approach to researching these geometries, as it involves subjecting the ferrofluid to a strong magnetic field [29–33]. Many researchers have been working on hybrid ferrofluids (HF_{fd}) with porous surfaces. Rauf *et al.*, [34] investigate ferrofluid flow across a rotating disk with alternating magnetic fields, studying heat transfer and three-dimensional flow. Zainodin *et al.*, [35] explore hybrid ferrofluid behavior under a variety of physical circumstances, finding that adding nanoparticles increases heat and mass transfer rates while also being impacted by slip boundary conditions and chemical reaction order. Sharma *et al.*, [36] study the channeling effects in complex porous media with stretchy, convectively heated walls, studying flow and temperature modulations in HF_{fd} and demonstrating the dominance of convection transfer in heterogeneous porous media. Rosli *et al.*, [37] explored HF_{fd} heat transfer across permeability stretched sheets, taking into account thermal radiation impacts. Idris *et al.*, [38] model the heat transfer flow of a HF_{fd} (Fe_3O_4 - $CoFe_2O_4$ /water) across a movable surface, including MHD, viscous dissipation, and suction/injection influences. Zhu *et al.*, [39]

revealed higher thermal conductivities in aqueous nanofluids than in other oxide-based equivalents, which they attributed to nanoparticle clustering and alignment, with no magnetic effects seen. Shah *et al.*, [40] analyzed theoretical squeeze film behavior in journal bearings using several ferrofluid flow models, generating formulas for pressure, load capacity, and reaction time. Raza *et al.*, [41] investigate ferrofluid dynamics with solid particles, nano-layers, and magnetic fields in porous disks, focusing on heat transfer. Chu *et al.*, [42] evaluated the thermal behavior of hybrid nanomaterials in a variety of applications by numerically assessing a nanofluid including four different nanoparticle types under nonuniform heat and an angled magnetic field on a stretched surface. Iqbal *et al.*, [43] investigated the effect of axisymmetric flow and heat transmission on different forms of copper nanoparticles across an unstable radial stretching surface, which was a unique field with no prior study. Sadiq *et al.*, [44] investigated nanofluid flow at a stagnation point on a lubricated stretched surface, employing the Legendre wavelet spectral collocation method to examine the influence of power-law lubricants on fluid velocity and temperature. Maatoug *et al.*, [45] explored the thermal impact of nanofluid on lubricated stretching surfaces at a stagnation point. They used the variational iteration approach to study lubrication, which has implications for polymer processing and hydraulic systems. Yang *et al.*, [46] explored heat transfer using hybrid nanofluids, examining various forms and parameters such as slip mechanism and magnetic force, and discovered increased thermal rates for blade-shaped titanium oxide-ethylene glycol breakdown. Alsallami *et al.*, [47] investigated the effect of a Williamson hybrid nanofluid on engine oil thermal characteristics using analytical and computational approaches. Raza *et al.*, [41] investigate single-phase simulations of magnetized metallic nanoparticles in fluid systems, focusing on heat and mass transfer using numerical techniques and fractal interfacial theory. Qureshi *et al.*, [48] investigated hybrid nanofluid flow containing ferroxidase and carbon nanotubes, taking into account magneto-hydrodynamics, Reynolds number effects, heat radiation, and porosity.

Based on recent literature, no prior research has explored the heat transfer characteristics of Newtonian liquids flowing through a channel under suction or injection conditions across two porous movable surfaces. The study is motivated by the unique ability of ferromagnetic nanoparticles to enhance thermal efficiency in the host fluid, which holds promise for various real-life applications [49, 50]. The objective of this study is to numerically investigate the time-dependent, two-dimensional (2D) magnetohydrodynamic (MHD) behavior of a hybrid ferrofluid (Fe_3O_4 - $CoFe_2O_4/H_2O + EG$) flowing over a porous surface, taking into account nonuniform heat source/sink conditions and thermal radiation. The numerical solutions are obtained by transforming the partial differential equations (PDEs) into nonlinear ordinary differential equations (ODEs) using similarity transformations. We employ the 4th-order Runge-Kutta method (RK) to solve the coupled nonlinear ordinary differential equations, using the shooting technique implemented with Mathematica software. The study presents results for various physical parameters in tabular and graphical formats, with a focus on the skin friction coefficient and Nusselt number, and also illustrates velocity and temperature profiles.

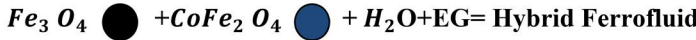
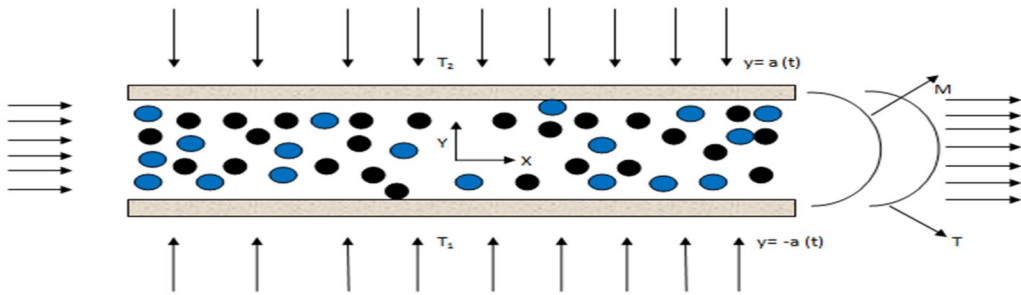
2. Mathematical formulation

Consider the laminar, unsteady, incompressible flow of a HF_{fd} ($Fe_3O_4 - CoFe_2O_4 / H_2O + EG$) across a two porous channel. This analysis includes irregular heat source/sink and thermal radiation effects, all within the influence of a magnetic field. The induced magnetic field is considered insignificant in comparison to the forced field. The fluid under investigation, referred to as the base fluid, is presumed to be Newtonian, specifically water. A thermal equilibrium is assumed to be present between the base fluid and magnetized nanoparticles. Table 1 explains the two different magnetized nanoparticles (Fe_3O_4 and $CoFe_2O_4$) and base fluid (water + EG (50–50%)) thermo-physical properties. The coordinate system is defined with the x-axis and y-axis positioned horizontally and vertically, respectively, as illustrated in Figure 1. In this flow geometry, the u velocity varies along the

Table 1. Thermophysical properties of HF_{fd} : density, heat capacity, viscosity, and thermal conductivity [51].

Properties	HF_{fd} ($Fe_3 O_4 - CoFe_2 O_4 / H_2 O + EG$)
Density ($kg\ m^{-3}$)	$\rho_{hffd} = \varphi_1 \rho_{s_1} + \varphi_2 \rho_{s_2} + (1 - (\varphi_1 + \varphi_2)) \rho_{bf}$
Heat capacity ($J\ K^{-1}$)	$(\rho c_p)_{hffd} = \varphi_1 (\rho c_p)_{s_1} + \varphi_2 (\rho c_p)_{s_2} + (1 - \varphi_1 - \varphi_2) (\rho c_p)_{bf}$
Viscosity (Nsm^{-1})	$\mu_{hffd} = \frac{\mu_{bf}}{(1 - \varphi_1 - \varphi_2)^{2.5}}$
Thermal Conductivity ($W\ K^{-1}m^{-1}$)	$k_{hffd} = \frac{k_{s_2} + (N-1)k_{hfd} - (N-1)\varphi_2(k_{hfd} - k_{s_2})}{k_{s_2} + (N-1)k_{hfd} + \varphi_2(k_{hfd} - k_{s_2})} k_{hfd}$
Where	$k_{hfd} = \frac{k_{s_1} + (N-1)k_{bf} - (N-1)\varphi_1(k_{bf} - k_{s_1})}{k_{s_1} + (N-1)k_{bf} + \varphi_1(k_{bf} - k_{s_1})} k_{bf}$

Case 1 (suction):



Case 2 (injection):

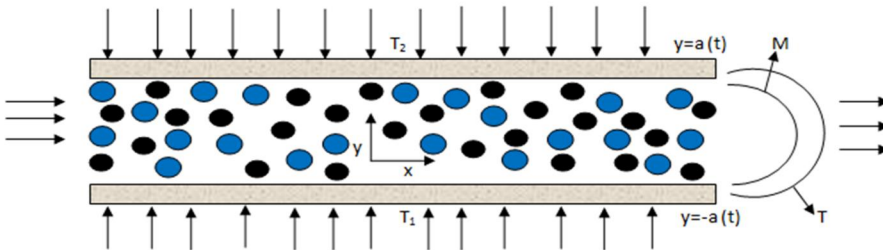


Figure 1. Physical model.

x-axis, while the v velocity varies along the y -axis across the porous channel. The T_1 and T_2 represent the bottom and top temperatures of the suction and injection channels. The equations governing the flow are presented based on the aforementioned assumptions:

Equation of continuity:

$$\frac{\partial u}{\partial x} + \frac{\partial v}{\partial y} = 0, \quad (1)$$

Equation of momentum:

$$\frac{\partial u}{\partial t} + u \frac{\partial u}{\partial x} + v \frac{\partial u}{\partial y} = -\frac{p_x}{\rho_{hffd}} + \nu_{hffd} \left(\frac{\partial^2 u}{\partial x^2} + \frac{\partial^2 u}{\partial y^2} \right) - \frac{\sigma_e B^2}{\rho_{hffd}} u, \quad (2)$$

$$\frac{\partial v}{\partial t} + u \frac{\partial v}{\partial x} + v \frac{\partial v}{\partial y} = -\frac{p_y}{\rho_{hffd}} + \nu_{hffd} \left(\frac{\partial^2 v}{\partial x^2} + \frac{\partial^2 v}{\partial y^2} \right), \quad (3)$$

Energy equation:

$$\left(\rho c_p \right)_{hffd} \left(\frac{\partial T}{\partial t} + u \frac{\partial T}{\partial x} + v \frac{\partial T}{\partial y} \right) = \left(k_{hffd} + \frac{16T_\infty^3 \sigma^*}{3k^*} \right) \frac{\partial T^2}{\partial y^2} + q'''. \quad (4)$$

In this context, k_{hffd} represents the thermal conductivity of the HF_{fd} , B denotes the external uniform magnetic field, σ^* is the Stefan–Boltzmann constant, k^* is the constant of mean absorption, σ_e denoted that the electric conductivity, p is the pressure term, T is the temperature, ρ_{hffd} stands for the density of the HF_{fd} , μ_{hffd} represents the dynamic viscosity, and, $\nu_{hffd} = \frac{\mu_{hffd}}{\rho_{hffd}}$ denotes the kinematic viscosity.

Boundary conditions are:

$$\begin{aligned} y = -a(t), u = 0, v = -Aa'(t), T = T_1, \text{ and} \\ y = a(t), u = 0, v = Aa'(t), T = T_2. \end{aligned} \quad (5)$$

The simulation setup includes boundary conditions dictating the fluid flow and temperature distribution. At $y = -a(t)$, horizontal velocity u is zero. In contrast, vertical velocity v is determined by the rate of change of $a'(t)$ and a wall permeability factor constant A . The bottom temperature is set to T_1 at this boundary. At $y = a(t)$, similar conditions apply, but with opposite velocity direction and top temperature set to T_2 . These conditions ensure accurate modeling of flow and heat transfer within the system.

Applying the following similarity transformation to Eqs. (1)–(4):

$$\eta = \frac{y}{a} \quad u = -\frac{xv_f}{a^2} F_\eta(\eta, t) \quad v = \frac{v_f}{a} F(\eta, t) \quad \theta = \frac{T - T_2}{T_1 - T_2} \quad (6)$$

Where A^* and B^* correspond to nonuniform heat/sink source, q''' is the nonuniform heat source provided by,

$$q''' = \frac{k_f u_w (T_1 - T_2)}{xv_f} \left(A^* f' + B^* \left(\frac{T - T_2}{T_1 - T_2} \right) \right) \quad (7)$$

With boundary condition

$$\eta = -1, F = -Ref, F_\eta = 0, \theta = 1, \quad (8)$$

And $\eta = 1, F = Ref, F_\eta = 0, \theta = 0$.

Here T_1 and T_2 (with $T_1 > T_2$) are bottom and top temperatures fixed channels respectively. Where $\alpha = \frac{aa'(t)}{v_f}$ the illustration that the wall expansion ratio, $Re = \frac{Aaa'(t)}{v_f}$ represented permeability Reynolds number, $M = \frac{\sigma_e B^2 a^2}{\mu_f}$ stand magnetic field, $R = \frac{(4)T_\infty^3 \sigma^*}{3K^* K_f}$ show by Radiation parameter, $\lambda = \left(\frac{a}{x} \right)^2$ symbolized film thickness parameter, $E = \frac{u_w x}{v_f}$ signified unsteadiness parameter and $Pr = \frac{(\mu c_p)_f}{k_f}$ denoted by Prandtl number. Therefore we have the equations below,

$$\frac{\nu_{hffd}}{\nu_f} F_{\eta\eta\eta\eta} + (3\alpha + F_\eta) F_{\eta\eta} + (\eta\alpha - Ref) F_{\eta\eta\eta} - \frac{a^2 F_{\eta\eta t}}{\nu_f} - M \frac{\rho_f}{\rho_{hffd}} F_{\eta\eta} = 0 \quad (9)$$

$$\begin{aligned} & \left(\frac{k_{hffd} k_{bf}}{k_{bf} k_f} + \frac{4}{3} R \right) \theta_{\eta\eta} + \lambda E(A^* f' + B^* \theta) + \left((1 - (\varphi_1 + \varphi_2)) + (\varphi_1) \left(\frac{(\rho c_p)_{s1}}{(\rho c_p)_f} \right) \right. \\ & \left. + (\varphi_2) \left(\frac{(\rho c_p)_{s2}}{(\rho c_p)_f} \right) \right) \text{Pr}(\alpha\eta - F)\theta_\eta - \frac{(\rho c_p)_{hffd} \nu_f}{k_f} \theta_t = 0 \end{aligned} \quad (10)$$

Finally, we set $F = f \text{ Re}$. when α is a constant, $f = f(\eta)$ and $\theta = \theta(\eta)$, which leads to $\theta_t = 0$ and $f_{\eta t} = 0$. We obtain the final result:

$$\frac{\nu_{hffd}}{\nu_f} F_{\eta\eta\eta\eta} + (3\alpha + F_\eta) F_{\eta\eta} + (\eta\alpha - \text{Re}f) F_{\eta\eta\eta} - \frac{a^2 F_{\eta\eta t}}{\nu_f} - M \frac{\rho_f}{\rho_{hffd}} F_{\eta\eta} = 0 \quad (11)$$

$$\begin{aligned} & \left(\frac{k_{hffd} k_{bf}}{k_{bf} k_f} + \frac{4}{3} R \right) \theta_{\eta\eta} + \lambda E(A^* f' + B^* \theta) + \left((1 - (\varphi_1 + \varphi_2)) + (\varphi_1) \left(\frac{(\rho c_p)_{s1}}{(\rho c_p)_f} \right) \right. \\ & \left. + (\varphi_2) \left(\frac{(\rho c_p)_{s2}}{(\rho c_p)_f} \right) \right) \text{Pr}(\alpha\eta - \text{Re}f[\eta])\theta_\eta = 0 \end{aligned} \quad (12)$$

$$\begin{aligned} & \eta = -1, f = -1, f_\eta = 0, \theta = 1, \\ & \text{And, } \eta = 1, f = 1, f_\eta = 0, \theta = 0 \end{aligned} \quad (13)$$

2.1. Simulate and numerically apply the thermophysical properties of (HF_{fd})

The nonlinear ordinary differential Eqs. (11)–(12), which incorporate the thermophysical properties of HF_{fd} , are provided below:

$$\begin{aligned} & \left(\frac{1}{(1 - (\varphi_1 + \varphi_2))^{2.5} \left((1 - (\varphi_1 + \varphi_2)) + (\varphi_1) \left(\frac{\rho_{s1}}{\rho_{bf}} \right) + (\varphi_2) \left(\frac{\rho_{s2}}{\rho_{bf}} \right) \right)} \right) f''''[\eta] + f''''[\eta] (\alpha\eta - \text{Re}f[\eta]) \\ & + f''[\eta] \left(3\alpha + \text{Re}f'[\eta] \right) - \left(\frac{1}{\left((1 - \varphi_1 - \varphi_2) + \varphi_1 \left(\frac{\rho_{s1}}{\rho_{bf}} \right) + \varphi_2 \left(\frac{\rho_{s2}}{\rho_{bf}} \right) \right)} \right) M f''[\eta] = 0 \end{aligned} \quad (14)$$

$$\begin{aligned} & \left(\left(\frac{k_{s2} + (N-1)k_{ffd} - (N-1)\varphi_2(k_{ffd} - k_{s2})}{k_{s2} + (N-1)k_{ffd} + \varphi_2(k_{ffd} - k_{s2})} \right) \left(\frac{k_{s1} + (N-1)k_{bf} - (N-1)\varphi_1(k_{bf} - k_{s1})}{k_{s1} + (N-1)k_{bf} + \varphi_1(k_{bf} - k_{s1})} \right) + \frac{4}{3} R \right) \theta''[\eta] \\ & + \lambda E(A^* f' + B^* \theta) + \left((1 - (\varphi_1 + \varphi_2)) + (\varphi_1) \left(\frac{\rho_{cps1}}{\rho_{cpbf}} \right) + (\varphi_2) \left(\frac{\rho_{cps2}}{\rho_{cpbf}} \right) \right) \text{Pr}(\alpha\eta - \text{Re}f[\eta])\theta'[\eta] = 0 \end{aligned} \quad (15)$$

$$C_1 = \left(\frac{1}{(1 - (\varphi_1 + \varphi_2))^{2.5} \left((1 - (\varphi_1 + \varphi_2)) + (\varphi_1) \left(\frac{\rho_{s1}}{\rho_{bf}} \right) + (\varphi_2) \left(\frac{\rho_{s2}}{\rho_{bf}} \right) \right)} \right) \quad (16)$$

$$C_2 = \left(\frac{1}{\left((1 - \varphi_1 - \varphi_2) + \varphi_1 \left(\frac{\rho_{s1}}{\rho_{bf}} \right) + \varphi_2 \left(\frac{\rho_{s2}}{\rho_{bf}} \right) \right)} \right) \quad (17)$$

$$C_3 = \left((1 - (\varphi_1 + \varphi_2)) + (\varphi_1) \left(\frac{\rho_{cps1}}{\rho_{cpbf}} \right) + (\varphi_2) \left(\frac{\rho_{cps2}}{\rho_{cpbf}} \right) \right) \quad (18)$$

$$D_1 = \left(\frac{k_{s2} + (N-1)k_{ffd} - (N-1)\varphi_2(k_{ffd} - k_{s2})}{k_{s2} + (N-1)k_{ffd} + \varphi_2(k_{ffd} - k_{s2})} \right) \quad (19)$$

$$D_2 = \left(\frac{k_{s1} + (N-1)k_{bf} - (N-1)\varphi_1(k_{bf} - k_{s1})}{k_{s1} + (N-1)k_{bf} + \varphi_1(k_{bf} - k_{s1})} \right) \quad (20)$$

$$Q = D_1 D_2 \quad (21)$$

Substituting the values from Eqs. (16), (17), (18), (19), (20), and (21) into Eqs. (14) and (15) yields the final results.

$$C_1 f''''[\eta] + f'''[\eta](\alpha\eta - \text{Ref}[\eta]) + f''[\eta](3\alpha + \text{Ref}'[\eta]) - C_2 M f''[\eta] = 0 \quad (22)$$

$$\left(Q + \frac{4}{3}R \right) \theta''[\eta] + \lambda E(A^* f' + B^* \theta) + C_3 \text{Pr}(\alpha\eta - \text{Ref}[\eta]) \theta'[\eta] = 0 \quad (23)$$

2.2. Solution of problem

The numerical methods employed to solve the nonlinear ordinary differential equations include the Runge-Kutta methods and shooting technique. Runge-Kutta methods provide an efficient approach for solving ordinary differential equations, while the shooting technique is particularly useful for boundary value problems. These methods enable the conversion of partial differential equations into ordinary differential equations for numerical computation.

Before beginning this procedure, the following modifications should be implemented:

$$e_1^* = f[\eta], e_2^* = f'[\eta], e_3^* = f''[\eta], e_4^* = f'''[\eta], e_5^* = \theta[\eta], e_6^* = \theta'[\eta]. \quad (24)$$

Modify the model based on Eqs. (22), and (23).

$$f''''[\eta] = \frac{1}{C_1} (-\alpha(3f'' + \eta f''') + \text{Re}(ff'''' - f'f'')) + C_2 M f'', \quad (25)$$

$$\theta''[\eta] = \frac{1}{\left(Q + \frac{4}{3}R\right)} (\text{Pr}(2\text{Ref} - \alpha\eta)\theta' - \lambda E(A^* f' + B^* \theta)) \quad (26)$$

The method described is attained through the utilization of the substitution outlined in Eq. (24).

$$\begin{bmatrix} e_1^* \\ e_2^* \\ e_3^* \\ e_4^* \\ e_5^* \\ e_6^* \end{bmatrix} = \begin{bmatrix} e_2^* \\ e_3^* \\ e_4^* \\ \frac{1}{C_1} ((-\alpha(3e_3^* + \eta e_4^*) + \text{Re}(e_1^* e_4^* - e_2^* e_3^*) + C_2 M e_3^*)) \\ e_6^* \\ \frac{1}{e_1} \left(\frac{1}{\left(Q + \frac{4}{3}R\right)} (\text{Pr}(2\text{Re}e_1^* - \alpha\eta)e_6^* - \lambda E(A^* e_2^* + B^* e_7^*)) \right) \end{bmatrix}$$

Consequently, the initial condition is:

$$\begin{bmatrix} e_1^* \\ e_2^* \\ e_3^* \\ e_4^* \\ e_5^* \\ e_6^* \end{bmatrix} = \begin{bmatrix} -1 \\ 0 \\ 1 \\ 0 \\ 1 \\ 0 \end{bmatrix}$$

Additionally, Mathematica software is utilized to implement these numerical methods and solve the resulting ordinary differential equations. Mathematica offers powerful computational capabilities and provides a manageable situation for solving mathematical problems, making it well-suited for this task. The solver's syntax, `soll = [NDSolve[{eqn1, eqn2, bcs1, bcs2}, {f[η], f'[η], f''[η], θ[η], θ'[η], {η, -1, 1}}, Method -> {"Shooting", "StartingInitialConditions" -> {{f[-1] == 1, f'[-1] == 0, f''[-1] == 0, f'''[-1] == 0, θ[-1] == 1, θ'[-1] == 0}}]]],` the NDSolve function is used to encode equations systems 11–12. The top and bottom boundary conditions (13) are then incorporated into the `@OdeBC1=={f[-1]== -1, f'[-1]==0, f[1]==1, f'[1]==0};@OdeBC2=={θ[-1]==1,θ[1]==0};function handle`. The outcomes' initial approximation and grid locations are computed using ND Solve. When solving ordinary differential equations (ODEs), it is crucial to possess a starting approximation for the desired solution. If the initial guess is accurate, it should satisfy the boundary conditions and exhibit the behavior of the solution. The Shooting technique can yield the required outcomes even when commencing with an inadequate initial estimation, mitigating the original approximation's complexity. By making modest adjustments to the coefficients, we can obtain an initial approximation for the resolution of the problem. Hence, we consistently enhance the coefficients until they closely match the accurate values.

2.1.1. Practical and engineering interests

Physical quantities such as skin friction and Nusselt number are crucial to model equipment at the nanoscale in engineering applications. These parameters were calculated for both porous channels.

2.1.2. Skin friction coefficients

The skin friction coefficients of top and bottom porous channels are denoted by C_{f1} and C_{f-1} , respectively, and are defined as follows:

$$C_{f-1} = \frac{\zeta_y|_{\eta=-1}}{\rho_f(a'A)^2} = \frac{1}{Re_r(1 - \varphi_1 - \varphi_2)^{2.5}} f''(-1), \quad (27)$$

$$C_{f1} = \frac{\zeta_y|_{\eta=1}}{\rho_f(a'A)^2} = \frac{1}{Re_r(1 - \varphi_1 - \varphi_2)^{2.5}} f''(1)$$

Here, $Re_r = \left(\frac{a}{r}\right) \frac{1}{(Re)^2}$ signifies the local Reynolds number, while ζ_y represents the shear stresses at the bottom and top porous channels in the radial direction, respectively.

$$\zeta_y = \mu_{hffd} \left(\frac{\partial u}{\partial y} \right) \Big|_{\eta=-1} = \frac{\mu_{bf}}{(1 - \varphi_1 - \varphi_2)^{2.5}} \left(\frac{rv_f}{a^3} \right) f''(-1)$$

$$\zeta_y = \mu_{hffd} \left(\frac{\partial u}{\partial y} \right) \Big|_{\eta=1} = \frac{\mu_{bf}}{(1 - \varphi_1 - \varphi_2)^{2.5}} \left(\frac{rv_f}{a^3} \right) f'''(1)$$

2.1.3. Nusselt numbers

The Nusselt coefficients for heat transfer rates at the top and bottom porous channels, designated as Nu_{y-1} and Nu_{y1} respectively, are computed as follows:

$$\begin{aligned} Nu_{y-1} &= \frac{ad_y}{\kappa_f(T_1 - T_2)} \Big|_{\eta=-1} = -\frac{k_{hffd}}{k_f} \theta'(-1) \\ u_{y1} &= \frac{cd_y}{\kappa_f(T_1 - T_2)} \Big|_{\eta=1} = -\frac{k_{hffd}}{k_f} \theta'(1) \end{aligned} \tag{28}$$

Here, the heat flux is represented by d_y , defined as follows:

$$\begin{aligned} d_y|_{\eta=-1} &= -k_{hffd} \left(\frac{\partial T}{\partial y} \right) \Big|_{\eta=-1} = -\frac{(T_1 - T_2)}{c} k_{hffd} \theta'(-1) \\ d_y|_{\eta=1} &= -k_{hffd} \left(\frac{\partial T}{\partial y} \right) \Big|_{\eta=1} = -\frac{(T_1 - T_2)}{c} k_{hffd} \theta'(1) \end{aligned}$$

Where

$$Re = \frac{Aaa'(t)}{v_f}.$$

3. Results and discussion

We utilized the numerical shooting technique to solve the nonlinear ordinary differential Eqs. (22)–(23), ensuring the incorporation of suitable boundary conditions. Additionally, we conducted a study to explore the physical factors influencing axial velocity ($f(\eta)$), radial velocity ($f'(\eta)$), and temperature profiles ($\theta(\eta)$), while also analyzing the associated flow behavior. Throughout the study, we considered flow parameters such as Reynolds number (Re), radiation parameter (R), expansion ratio (α), Prandtl number (Pr), magnetic field (M), film thickness parameter (λ), unsteadiness (E), volume fractions (φ_1 and φ_2), and nonuniform heat sink/source (A^* and B^*). The results, as depicted in the tables and graphs, exhibit consistent values. Table 2 displays the thermophysical properties of HF_{fd} (water + EG + Fe_3O_4 + $CoFe_2O_4$). The analysis covers estimation ranges with parameter values assigned as follows: $-4 \leq Re \leq 4$, $-5 \leq \alpha \leq 5$, $1 \leq A^* \leq 2.5$, $1 \leq B^* \leq 2.5$, $6.2 \leq B^* \leq 8.5$, $1 \leq R \leq 17$, $1 \leq M \leq 27$, $1 \leq \lambda \leq 27$. Table 3 reveals that increasing the expanding/contracting parameter (α) results in a decrease in shear stress and heat transfer rate, while maintaining constant values for $Re, R, Pr, M, \varphi_1, \varphi_2, A^*$ and B^* . Moreover, elevating the Re reduces shear stress but enhances heat transfer rate, assuming constant physical parameters ($\alpha, R, Pr, M, \varphi_1$, and φ_2). By varying the R to evaluate its influence on heat transfer rate, it is observed that an increase in R leads to higher heat transfer flow in a HF_{fd}

Table 2. Thermo-physical properties of base fluids and two different magnetic nanoparticles [50].

Title	H_2 O + EG 50%	$Fe_3O_4(\varphi_1)$	$CoFe_2O_4(\varphi_2)$
ρ (kg m^{-3})	1056	5180	4907
C_p (J k $g^{-1}K^{-1}$)	3288	670	700
κ ($wm^{-1}K^{-1}$)	0.425	9.7	3.7

Table 3. Shear stress ($f''(-1)$) and heat transfer ($\theta'(-1)$) flow of hybrid ferrofluid under the influence of various physical parameters $\alpha, Re, R, Pr, M, \varphi_1, \varphi_2, A^*$ and B^*

α	Re	R	Pr	M	φ_1	φ_2	A^*	B^*	$ f''(-1) $	$ \theta'(-1) $
1	-1	1	6.2	1	0.01	0.01	1	1	2.42023	0.067505
2									1.81056	0.020759
3									1.27018	0.006130
4									0.806850	0.0017242
1	-1	1	6.2	1	0.01	0.01	1	1	2.42023	0.0675049
	-0.5								2.40494	0.1294080
	0								2.38788	0.252907
	0.5								2.36870	0.499658
1	-1	1	6.2	1	0.01	0.01	1	1	2.42023	0.0675049
		2							2.42023	0.1441741
		3							2.42023	0.2044352
		4							2.42023	0.248495
1	-1	1	6.2	1	0.01	0.01	1	1	2.42023	0.0675049
			7.0						2.42023	0.0480739
			7.8						2.42023	0.0341860
			8.5						2.42023	0.025266
1	-1	1	6.2	1	0.01	0.01	1	1	2.42023	0.0675049
				2					2.41127	0.0675049
				3					2.40319	0.0675049
				4					2.39597	0.0675049
1	-1	1	6.2	1	0.01	0.01	1	1	2.42023	0.0675049
					0.02		1.3		2.40178	0.0631698
					0.03		1.9		2.3869	0.0591302
					0.04		2.3		2.37536	0.0553679
1	-1	1	6.2	1	0.01	0.01	1	1	2.42023	0.0675049
								0.02	2.40319	0.0639442
								0.03	2.38957	0.0606051
								0.04	2.37913	0.0574725
1	-1	1	6.2	1	0.01	0.01	1	1	2.42023	0.0675049
							1.3		2.42023	0.076571
							1.9		2.42023	0.0955971
							2.3		2.42023	0.106611
1	-1	1	6.2	1	0.01	0.01	1	1	2.42023	0.0675049
								1.4	2.42023	0.0586946
								1.8	2.42023	0.0512072
								2.4	2.42023	0.0425598

Table 4. Influence of radiation parameter (R) on Nusselt number (Nu) for injection/suction Reynolds number (Re).

R	$Re = 4$	$Re = -4$
	$ Nu _{\eta=-1}$	$ Nu _{\eta=-1}$
1	0.832884	0.000016
4	0.665395	0.014207
7	0.606438	0.062349
10	0.578133	0.116417
13	0.561646	0.163553
17	0.548079	0.213561

with a lower porous channel. As the values of the Pr increase, the flow rate of heat transfer decreases on a lower porous channel. Additionally, an increase in the M leads to a decrease in shear stress. Physically, raising the values of the irregular heat source/sink parameters (A^* and B^*) served as a stimulant for heat generation inside the flow. Consequently, it was observed that raising the fluid temperature occurred with an increase in parameter A^* while enhancing parameter B^* led to a reduction in the flow rate of heat transfer. Table 4 shows that the R affects the Nu at a constant Re in two different circumstances. Firstly, at $Re = 4$, the heat transfer flow rate decreases, whereas at $Re = -4$, the behavior of the HF_{fd} enhances in Nusselt number (Nu), particularly at the lower porous channel. Table 5 illustrates the relationship between the R and the

Table 5. Impact of radiation parameter (R) on Nusselt number (Nu) for expanding/contracting ratio (α).

R	$\alpha = 2$	$\alpha = -2$
	$ Nu _{\eta=1}$	$ Nu _{\eta=1}$
1	0.0002216	0.188095
4	0.0824763	0.260795
7	0.1855250	0.346616
10	0.2530871	0.387561
13	0.2978954	0.411337
17	0.3344662	0.429311

Table 6. Magnetic field parameter (M) impact on shear stress $|f''(-1)|$ for expanding/contracting ratio (α).

M	$\alpha = 2$	$\alpha = -2$
	$ f''(-1) $	$ f''(-1) $
1	0.143404	6.73890
2	0.584674	6.90321
3	1.164871	7.05929
4	1.645382	7.20813
5	2.054773	7.35051
6	2.411232	7.48711

Table 7. Numerical impact of the film thickness parameter λ in the flow of heat transfer for a lower porous channel.

λ	$Re = 1$	$Re = -1$
	$ \theta'(-1) $	$ \theta'(-1) $
1	0.25541	0.01879
3	0.67266	0.08496
5	1.71803	0.25278
7	2.73599	0.50102

Table 8. Impact of unsteadiness (E) and film thickness parameter (λ) on heat transfer in upper porous channels: Numerical comparison of ferrofluids and HF_{fd}

E	λ	Ferrofluid	Hybrid ferrofluid
		$ \theta'(1) _{\phi_1=0.04}$	$ \theta'(1) _{\phi_1=\phi_2=0.02}$
0.1	0.5	0.937865	0.943586
0.2		0.991332	0.997741
0.3		1.042421	1.049533
0.4		1.091074	1.098791
0.1	0.6	0.948743	0.954605
	0.7	0.959532	0.965531
	0.8	0.970221	0.976362
	0.9	0.980823	0.987091

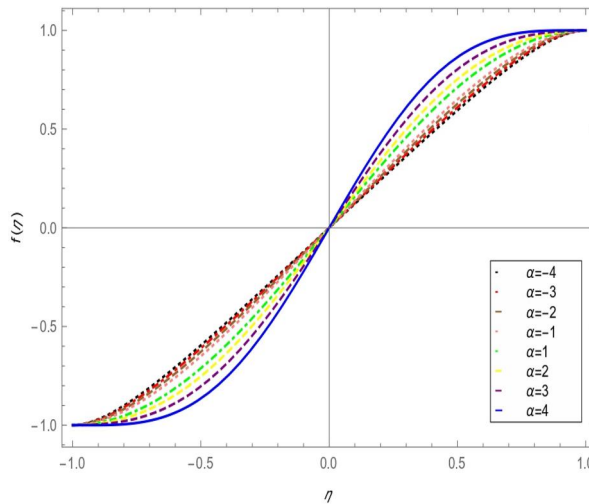
Nu for a constant α . An increase in R results in a higher Nu at the top porous channel for constant α values of 2 and -2 . Table 6 displays the impact of the M on the lower shear stress ($|f''(-1)|$) for two different values of α . Maintaining α constant at -2 and 2, an increase in the values of M leads to a gradual rise in the $|f''(-1)|$ in both cases, notably on the bottom porous channel. Table 7 demonstrates the effect of the λ on the thermal transfer rate for various Re . It is observed that in both cases of $Re = 1$ and $Re = -1$, the heat transfer rate increases with a larger λ . Physically, an increase in λ contradicts the motion of the liquid. This discrepancy may lead to an improvement in heat transfer within the fluid. Table 8 illustrates the impact of E and λ on heat transfer in the upper porous channel, comparing numerical values for two different fluids: Ferrofluid and HF_{fd} , while keeping other parameters constant. As the values of E and λ increase,

Table 9. Comparative assessment of shear stress and heat transfer at $\varphi_1 = \varphi_2 = 0.06$, $M = 1$, $\alpha = -1$, and $Pr = 6.2$: Our findings versus Qureshi *et al.*, [49].

Re	Qureshi <i>et al.</i> , [49] $f''(-1)$	Present work $f''(-1)$	Qureshi <i>et al.</i> , [49] $\theta'(-1)$	Present work $\theta'(-1)$
-1	4.19168	4.19171	-0.36988	-0.36985
-0.5	4.40338	4.40340	-0.968884	-0.968882
0	4.64876	4.64879	-1.98464	-1.98461
0.5	4.93215	4.93218	-3.26874	-3.26871
-1	5.25781	5.25783	-4.63023	-4.63021

Table 10. Validating the current numerical and stability solutions with data using a step size of 0.2.

η	$f(\eta)$	$f'(\eta)$	$f''(\eta)$
-1.0	-1.	$1.7913730 \times 10^{-16}$	3.000684842496
-0.8	-0.943646158614	0.5441245126760	2.4204693228282
-0.6	-0.7906755822441	0.9640885589350	1.7770186618229
-0.4	-0.5665604431803	1.2561458113446	1.14990902470936
-0.2	-0.2963014140511	1.42696027068749	0.5651448367838
0	-0.003332761448756	1.48425987373347	0.01060685772842
0.2	0.2963014140511	1.42696027068749	-0.5651448367838
0.4	0.5665604431803	1.2561458113446	-1.14990902470936
0.6	0.7906755822441	0.9640885589350	-1.7770186618229
0.8	0.943646158614	0.5441245126760	-2.4204693228282
1.0	1.	$1.7913730 \times 10^{-16}$	-3.000684842496


Figure 2. Effect of axial velocity profile along expansion ratio (α) for $Re = 1$, $R = 1$, $Pr = 6.2$, $M = 1$, $\varphi_1 = 0.02$, $\varphi_2 = 0.02$.

heat transfer improves in both fluids. It's worth noting that different nanoparticle volume fractions are adjusted in ferrofluid ($\varphi_1 = 0.04$) and HF_{fd} ($\varphi_1 = \varphi_2 = 0.04$). Our analysis reveals that the heat transfer rate is significantly better in HF_{fd} ($Fe_3O_4-CoFe_2O_4/H_2O + EG$) compared to ferrofluid ($Fe_3O_4/H_2O + EG$). Table 9 provides a contrast between our results and those from a prior study conducted by Qureshi *et al.*, [49], utilizing fixed parameters such as $\alpha = -1$, $\varphi_1 = \varphi_2 = 0.06$, $M = 1$, and $Pr = 6.2$. Additionally, Table 10 demonstrates the verification of our current research, exhibiting a step size of approximately 0.2. Figure 2 explores the influence of the α on the axial velocity profile ($f(\eta)$). Our analysis reveals that as the flow parameter α increases, the influence of the axial velocity diminishes in the bottom porous channel but intensifies in the top porous channel across momentum boundary layer thicknesses. Physically, This indicates that

higher α values lead to a redistribution of flow, enhancing velocity in the upper regions while reducing it in the lower regions of the channel. **Figure 3** illustrates the influence of the expansion ratio (α) on the streamlined radial velocity profile ($f'(\eta)$). The analysis shows that as α increases, $f'(\eta)$ rises at the center point, indicating a higher radial velocity. However, this radial velocity progressively decreases toward both the top and bottom porous channels, suggesting that the effect of the expansion ratio is most pronounced at the center and diminishes toward the boundaries. The analysis in **Figure 4** illustrates the physical significance of the α on the temperature profile ($\theta(\eta)$). As α changes from negative to positive values, the heat transfer rate within $\theta(\eta)$ maximizes at the top porous channel and decreases at the bottom porous channel. Physically, this means that positive α values enhance the thermal boundary layer's thickness at the top, leading to more efficient heat transfer, while at the bottom, the thermal boundary layer becomes thinner, reducing the heat transfer rate. **Figure 5**, we explore the influence of Re on the axial velocity

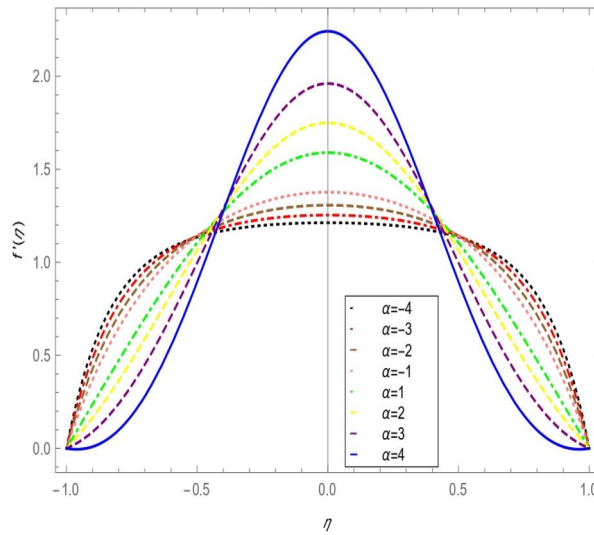


Figure 3. Effect of radial velocity profile along expansion ratio (α) for $Re = 1, R = 1, Pr = 6.2, M = 1, \varphi_1 = 0.02, \varphi_2 = 0.02$.

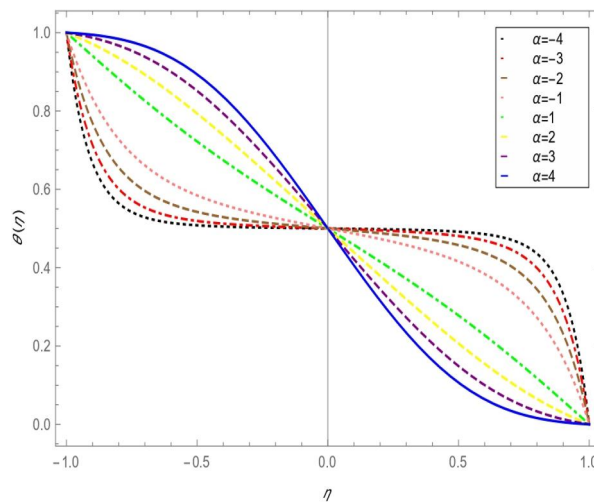


Figure 4. Effect of temperature profile along expansion ratio (α) for $Re = 1, R = 1, Pr = 6.2, M = 1, \varphi_1 = 0.02, \varphi_2 = 0.02$.

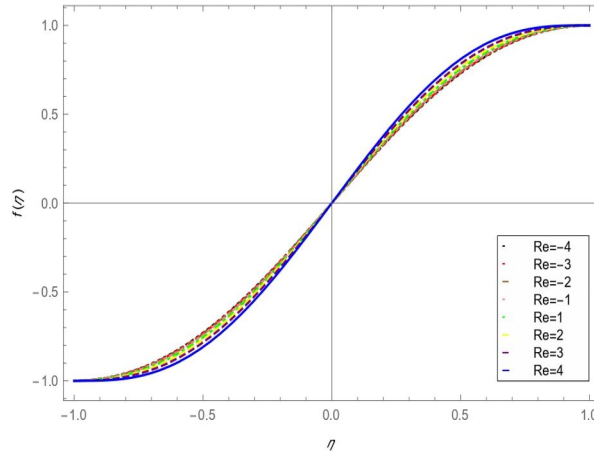


Figure 5. Effect of axial velocity profile along reynold number (Re) for $\alpha = 2, R = 1, Pr = 6.2, M = 1, \varphi_1 = 0.04, \varphi_2 = 0.04$.

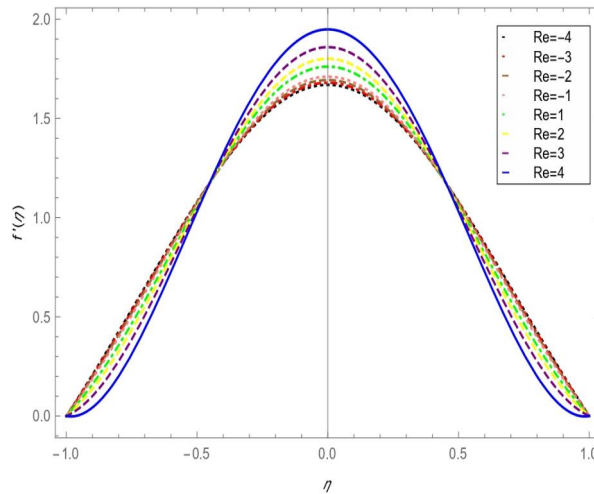


Figure 6. Effect of radial velocity profile along reynold number (Re) for $\alpha = 2, R = 1, M = 1, \varphi_1 = 0.04, \varphi_2 = 0.04$.

profile ($f(\eta)$), while keeping the $\alpha, R, Pr, M, \varphi_1$ and φ_2 constant. Notably, the $f(\eta)$ exhibits a minimum at the bottom porous channel, gradually increasing toward the wall's midpoint, and peaking at the top porous channel. **Figure 6** illustrates the influence of the Re on the $f'(\eta)$. Physically, the Reynolds number represents the ratio of inertial forces to viscous forces in a fluid flow system. For flow through a permeable channel, such as a porous channel, the Reynolds number helps predict the smoothness of the flow. When the Reynolds number is less than 2000, the flow through the medium is characterized by laminar flow, which is smooth and free of turbulence, with parallel and uniform layers. In essence, a low Reynolds number indicates that the flow within the channel is orderly and consistent, with limited fluid mixing or diffusion. The $f'(\eta)$ values are minimal at the bottom porous channel, rise toward the wall's midpoint to attain a peak, and then decline toward the top porous channel. From **Figure 7**, it is evident that the impact of Re on the temperature profile ($\theta(\eta)$) is significant. The heat transfer rate of $\theta(\eta)$ reaches its maximum at the bottom porous channel and progressively decreases toward the top porous channel when Re values are larger, regardless of whether they are zero or greater. This result suggests that there is a commensurate modification in the $\theta(\eta)$ within the flow as the Re increases.

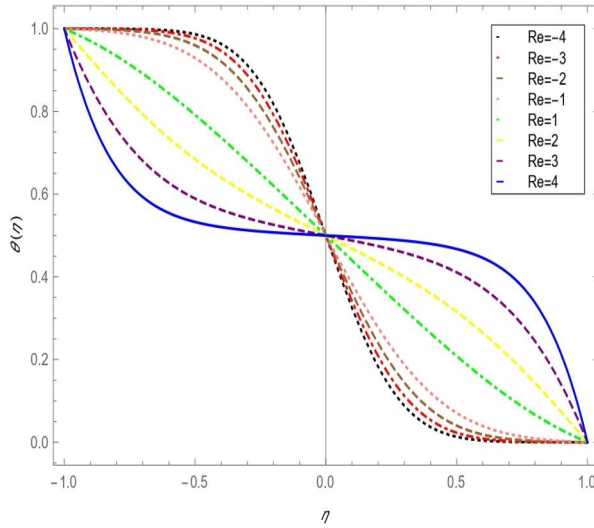


Figure 7. Effect of temperature profile along reynold's number (Re) for $\alpha = 2, Pr = 6.2, R = 1, \varphi_1 = 0.04, \varphi_2 = 0.04$.

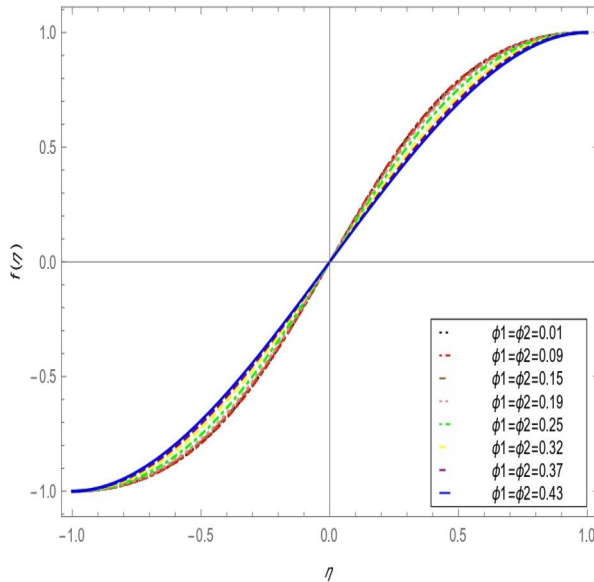


Figure 8. Effect of axial velocity profile along volume fraction ($\varphi_1 = \varphi_2$) for $\alpha = 5, Re = -4, R = 3, Pr = 6.2, M = 1$.

The variation profile appears to be asymmetrical, suggesting nonuniform heat distribution across the channel. These results are consistent while maintaining the parameters α, Pr, R, φ_1 and φ_2 constant. **Figure 8** demonstrates how the $f'(\eta)$ varies with the volume fractions (φ_1 and φ_2). It was noted that the fluid velocity increases with the volume fraction of HF_{fd} . However, contrasting results were observed at both porous surfaces' momentum boundary layer thickness. Additionally, the $f'(\eta)$ exhibits a higher value at the middle of the wall compared to both porous channels. The $f'(\eta)$ is also influenced by changes in the volume fraction (φ_1 and φ_2), as depicted in **Figure 9**. **Figure 10** elucidates the influence of volume fractions (φ_1 and φ_2) on the temperature profile ($\theta(\eta)$). Physically, the both nanoparticles volume fraction refers to the obstruction encountered by fluid as it traverses through a pipe or channel, stemming from the interaction

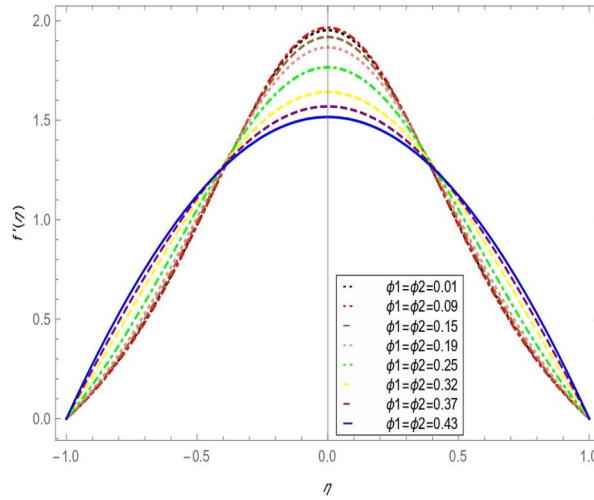


Figure 9. Effect of radial velocity profile along volume fraction ($\varphi_1 = \varphi_2$) for $\alpha = 5, Re = -4, R = 1, M = 1$.

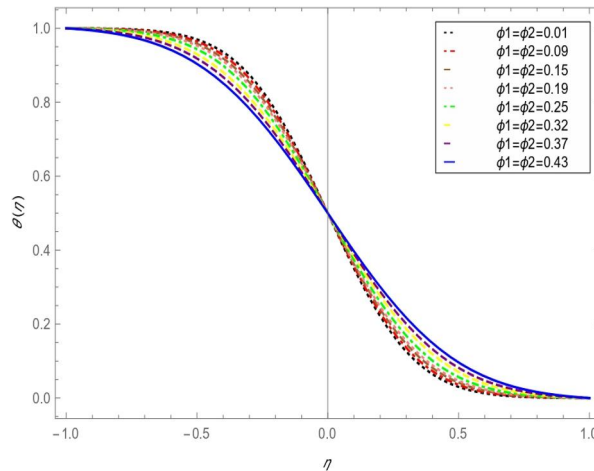


Figure 10. Effect of temperature profile along volume fraction ($\varphi_1 = \varphi_2$) for $\alpha = 5, Re = -4, R = 1, Pr = 6.2, M = 1$.

between the fluid and the surface it flows over. This resistance arises from the fluid's internal friction and is proportional to both its velocity and viscosity. The analysis uses constant variables of $\alpha = 5, Pr = 6.2, Re = -4$, and $M = 1$. Maintaining these values constant while adjusting φ_1 and φ_2 , it is noted that the thermal boundary layer width is larger at the top porous channel and minimal at the bottom porous channel within the channel.

Figure 11 portrays the influence of the M on the axial velocity profile ($f(\eta)$). It was determined that escalating the values of M enhances the performance of the hybrid ferrofluid at the bottom channel $f(-1)$ while diminishing it at the top channel $f(1)$, affecting both momentum boundary layer thicknesses. **Figure 12** depicts the impact of the M parameters on the radial velocity profile. ($f'(\eta)$). The improved performance is credited to the influence of the opposing force, known as the Lorentz force, associated with a strong magnetic strength denoted as M . When a magnetic field is applied to HF_{fd} models, it is assumed to be perpendicular to the flow, resulting in reduced mobility of magnetized nanoparticles. This reduction in mobility is further induced by Lorentz forces, represented as negative forces in dimensional momentum equations, contributing to the decreased motion of magnetized nanoparticles in HF_{fd} . The $f'(\eta)$ exhibits a

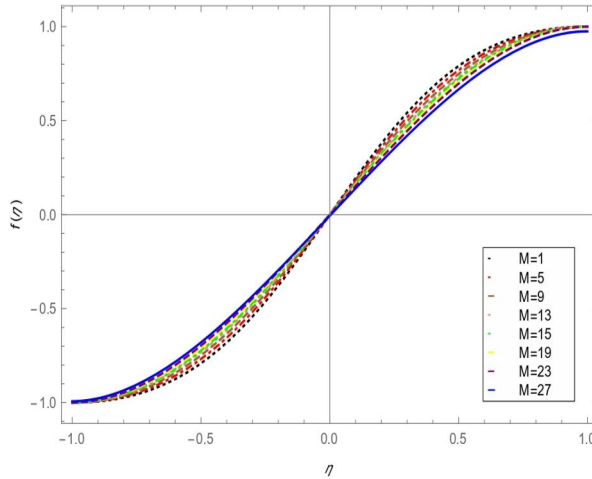


Figure 11. Effect of axial velocity profile along the magnetic field (M) for $\alpha = 5, Re = -4, R = 1, Pr = 6.2, \varphi_1 = 0.03, \varphi_2 = 0.03$.

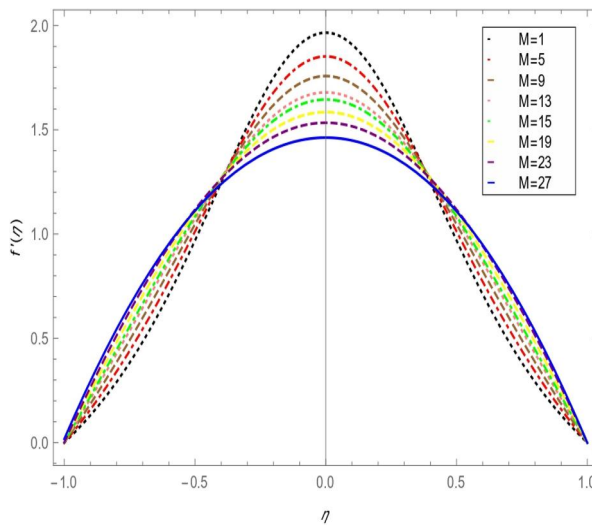


Figure 12. Effect of radial velocity profile along the magnetic field (M) for $\alpha = 5, Re = -4, R = 1, Pr = 6.2, \varphi_1 = 0.03, \varphi_2 = 0.03$.

minimum value at the bottom porous surface, gradually increasing toward the middle of the wall, and then decreasing again toward the top porous surface. The values of $\alpha, Re, \varphi_1, \varphi_2, R$ and Pr remain fixed during the process of calculation. **Figure 13** indicates that the Pr effects the temperature profile ($\theta(\eta)$). As the Pr increases, representing the ratio of momentum diffusivity to thermal diffusivity in a fluid, the heat transfer characteristics change distinctly. Near the lower boundary, where fluid flow is reduced, this indicates a thicker thermal boundary layer, which hinders heat transfer efficiency. Conversely, near the upper boundary, where fluid flow is enhanced, the thermal boundary layer thickness, facilitating more efficient heat transfer. **Figure 14** indicates the implications of altering the R on the temperature profile ($\theta(\eta)$). The diagram displays computations conducted with eight different values of R . It is generally understood that radiation is a thermal transfer phenomenon in which energy is radiated by liquid particles, resulting in further heat generation in the flow. As a result, we found an increase in the thermal field at higher R values. The thermal transfer rate is influenced by the gradient in temperature and the properties of

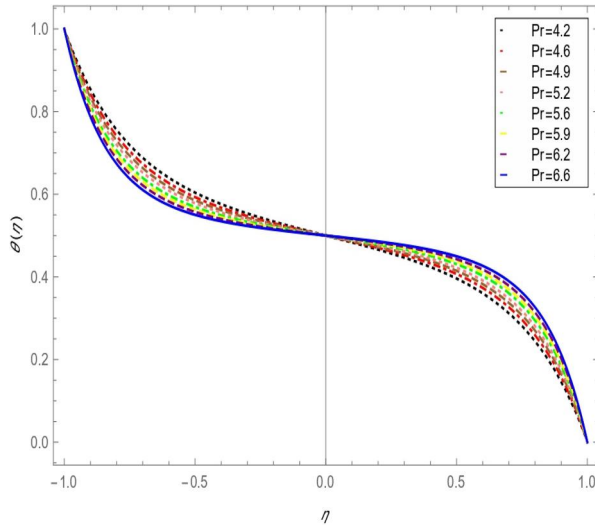


Figure 13. Effect of temperature profile along prandtl number (Pr) for $\alpha = -1, Re = 4, R = 3, \varphi_1 = 0.01, \varphi_2 = 0.01$.

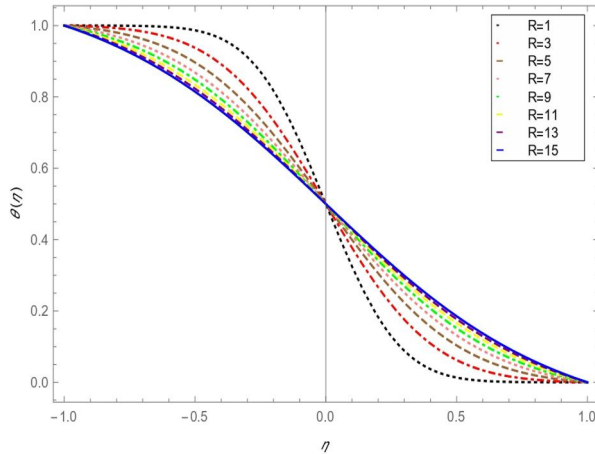


Figure 14. Effect of temperature profile along radiation parameter (R) for $\alpha = 2, Re = -4, Pr = 6.2, M = 1, \varphi_1 = 0.02, \varphi_2 = 0.02$.

the porous medium. At the bottom porous channel $\theta(-1)$, the temperature gradient is larger due to the initial contact with the heat source, resulting in a higher thermal transfer rate. As the heat moves toward the center of the wall, the gradient decreases, leading to a lower heat transfer rate. Finally, at the top porous channel $\theta(1)$, the gradient is at its smallest, resulting in the lowest thermal transfer rate. This distribution aligns with the principles of heat transfer in porous media.

4. Conclusion

This computational study explores the time-dependent, two-dimensional, incompressible magnetohydrodynamic (MHD) flow of HF_{fd} (water + EG + Fe_3O_4 + $CoFe_2O_4$) over two stretching surfaces with nonuniform heat source/sink conditions, focusing on heat transfer phenomena. The study converts two-dimensional partial differential equations into a nonlinear ordinary differential equation using similarity transformations. It employs the 4th-order Runge-Kutta method to obtain numerical results (skin friction coefficient, Nusselt number) and graphical representations

(velocity profile, temperature profile). The effects of various parameters, such as the radiation parameter (R), nonuniform heat sink/source (A^* and B^*), magnetic field (M), Prandtl number (Pr), Reynold number (Re), and both nanoparticle volume fractions φ_1 and φ_2 , are examined. Here are some notable findings:

- Boosting the values of A^* enhances heat transfer, while raising B^* diminishes the flow dynamics of the hybrid ferrofluid on the bottom porous channel.
- Elevating the film thickness parameter (λ) amplifies the heat transfer rate on the bottom porous channel, regardless of whether Re is less than or greater than 0.
- As the Radiation parameter (R) rises, the Nusselt number increases on the upper porous channel for both cases when $\alpha < 0$ and $\alpha > 0$.
- Rising the magnetic field parameter (M) enhances the shear stress on the bottom porous channel for both expanding and contracting (α) cases.
- Elevating the values of M and α boosts the axial velocity profile near the lower channel while decreasing it near the upper porous channel.
- As Pr, R , and Re rise, the temperature profile exhibits reduced flow near the bottom porous channel and heightened flow near the upper porous channel.
- At higher values of M, α, Re, φ_1 , and φ_2 , the radial velocity profile decreases near the top and bottom porous channels, while fluid flow behavior is enhanced in the middle of the wall.
- Increased values of E and λ result in a much-improved heat transfer rate in HF_{fd} compared to traditional ferrofluids.

Acknowledgment

The authors extend their appreciation to the Deputyship for Research & Innovation, Ministry of Education in Saudi Arabia for funding this research work through project number ISP23-66.

Disclosure statement

No potential conflict of interest was reported by the author(s).

Future direction

This work can be further extended to explore various types of non-Newtonian fluid models, including Ellis nanofluids, micropolar nanofluids, and those incorporating motile microorganisms, to optimize heat and mass transfer rates. Additionally, these models could be expanded to include tetra nanoparticles for comprehensive investigation and analysis.

ORCID

Qadeer Raza  <http://orcid.org/0009-0008-4831-5606>

Ali J. Chamkha  <http://orcid.org/0000-0002-8335-3121>

References

- [1] T. Hayat, M. Ijaz Khan, M. Imtiaz, A. Alsaedi and M. Waqas, "Similarity transformation approach for ferromagnetic mixed convection flow in the presence of chemically reactive magnetic dipole," *Phys. Fluids*, vol. 28, no. 10, pp. 102003, 2016. DOI: [10.1063/1.4964684](https://doi.org/10.1063/1.4964684).
- [2] A. Zeeshan, A. Majeed and R. Ellahi, "Effect of magnetic dipole on viscous ferro-fluid past a stretching surface with thermal radiation," *J. Mol. Liq.*, vol. 215, pp. 549–554, 2016. DOI: [10.1016/j.molliq.2015.12.110](https://doi.org/10.1016/j.molliq.2015.12.110).

- [3] H. Sadrhosseini, A. Sehat and M. B. Shafii, "Effect of magnetic field on internal forced convection of ferrofluid flow in porous media," *Experim. Heat Transf.*, vol. 29, no. 1, pp. 1–16, 2016. DOI: [10.1080/08916152.2014.926431](https://doi.org/10.1080/08916152.2014.926431).
- [4] A. Khalid, I. Khan and S. Shafie, "Heat transfer in ferrofluid with cylindrical shape nanoparticles past a vertical plate with ramped wall temperature embedded in a porous medium," *J. Mol. Liq.*, vol. 221, pp. 1175–1183, 2016. DOI: [10.1016/j.molliq.2016.06.105](https://doi.org/10.1016/j.molliq.2016.06.105).
- [5] S. Z. Abbas, A. Bhandari, J. Ahmed, N. H. Abu-Hamdeh and S. Bezzina, "Flow and heat transfer of ferro nanofluid in a porous medium under the impact of a static magnetic field," *Waves Random Complex Media*, pp. 1–19, Dec. 2021. DOI: [10.1080/17455030.2021.2012302](https://doi.org/10.1080/17455030.2021.2012302).
- [6] A. Sehat, H. Sadrhosseini and M. B. Shafii, "Experimental study of internal forced convection of ferrofluid flow in porous media," *DDF*, vol. 348, pp. 139–146, 2014. DOI: [10.4028/www.scientific.net/DDF.348.139](https://doi.org/10.4028/www.scientific.net/DDF.348.139).
- [7] M. Saeed, B. Ahmad and Q. M. Ul Hassan, "Variable thermal effects of viscosity and radiation of ferrofluid submerged in porous medium," *Ain Shams Eng. J.*, vol. 13, no. 4, pp. 101653, 2022. DOI: [10.1016/j.asej.2021.101653](https://doi.org/10.1016/j.asej.2021.101653).
- [8] S. E. Borglin, G. J. Moridis and C. M. Oldenburg, "Experimental studies of the flow of ferrofluid in porous media," *Transp. Porous Media*, vol. 41, pp. 61–80, 2000. DOI: [10.1023/A:1006676931721](https://doi.org/10.1023/A:1006676931721).
- [9] M. R. Ilias, N. A. Rawi and S. Shafie, "MHD free convection flow and heat transfer of ferrofluids over a vertical flat plate with aligned and transverse magnetic field," *Indian J. Sci. Technol.*, vol. 36, no. 9, pp. 1–7, 2016. DOI: [10.17485/ijst/2016/v9i36/128543](https://doi.org/10.17485/ijst/2016/v9i36/128543).
- [10] M. Usman, M. Hamid, S. T. Mohyud Din, A. Waheed and W. Wang, "Exploration of uniform heat flux on the flow and heat transportation of ferrofluids along a smooth plate: comparative investigation," *Int. J. Biomath.*, vol. 11, no. 04, pp. 1850048, 2018. DOI: [10.1142/S1793524518500481](https://doi.org/10.1142/S1793524518500481).
- [11] Y. Sheikhnejad et al., "Experimental investigation and three-dimensional numerical analysis of ferroconvection through horizontal tube under magnetic field of fixed parallel magnet bars", *J. Heat Transfer*, vol. 10, no. 139, pp. 101703, Oct. 2017.
- [12] D. Ghosh, Meena, P. R. and P. K. Das, "Heat transfer from a ferrofluid during generalized Couette flow through parallel plates in the presence of an orthogonal magnetic field," *Int. J. Therm. Sci.*, vol. 164, pp. 106895, 2021. DOI: [10.1016/j.ijthermalsci.2021.106895](https://doi.org/10.1016/j.ijthermalsci.2021.106895).
- [13] W. Nessab, H. Kahalerras, B. Fersadou and D. Hammoudi, "Numerical investigation of ferrofluid jet flow and convective heat transfer under the influence of magnetic sources," *Appl. Therm. Eng.*, vol. 150, pp. 271–284, 2019. DOI: [10.1016/j.applthermaleng.2018.12.164](https://doi.org/10.1016/j.applthermaleng.2018.12.164).
- [14] S. Saleem, T. Abbas, H. Abutuqayqah, E. U. Haq and S. U. Khan, "Numerical simulation accompanied by an intelligent computing system for the chemical reaction of Casson nanofluid and radiative heat flux on a nonlinear stretching surface," *Alex. Eng. J.*, vol. 79, pp. 629–643, 2023. DOI: [10.1016/j.aej.2023.08.016](https://doi.org/10.1016/j.aej.2023.08.016).
- [15] B. Ahmad, S. Bibi, S. U. Khan, T. Abbas and A. Raza, "Bioconvective thermal transport of micropolar nanofluid with applications of viscous dissipation and micro-rotational features," *Waves Random Complex Media*, pp. 1–19, 2023. DOI: [10.1080/17455030.2023.2226769](https://doi.org/10.1080/17455030.2023.2226769).
- [16] S. Saleem, B. Ahmad, A. Naseem, M. B. Riaz and T. Abbas, "Mono and hybrid nanofluid analysis over shrinking surface with thermal radiation: a numerical approach," *Case. Stud. Therm. Eng.*, vol. 54, pp. 104023, 2024. DOI: [10.1016/j.csite.2024.104023](https://doi.org/10.1016/j.csite.2024.104023).
- [17] Q. Raza, et al., "Insight into dynamic of mono and hybrid nanofluids subject to binary chemical reaction, activation energy, and magnetic field through the porous surfaces," *Mathematics*, vol. 10, no. 16, pp. 3013, 2022. DOI: [10.3390/math10163013](https://doi.org/10.3390/math10163013).
- [18] S. Khalil, H. Yasmin, T. Abbas and T. Muhammad, "Analysis of thermal conductivity variation in magneto-hybrid nanofluids flow through porous medium with variable viscosity and slip boundary," *Case. Stud. Therm. Eng.*, vol. 57, pp. 104314, 2024. DOI: [10.1016/j.csite.2024.104314](https://doi.org/10.1016/j.csite.2024.104314).
- [19] Q. Raza, et al., "Mathematical modeling of nanolayer on biological fluids flow through porous surfaces in the presence of CNT," *Case. Stud. Therm. Eng.*, vol. 45, pp. 102958, May 2023. DOI: [10.1016/j.csite.2023.102958](https://doi.org/10.1016/j.csite.2023.102958).
- [20] R. E. Rosensweig, "Directions in ferrohydrodynamics," *J. Appl. Phys.*, vol. 57, no. 8, pp. 4257–64, 1985. DOI: [10.1063/1.334579](https://doi.org/10.1063/1.334579).
- [21] B. Hindebu Rikitu, O. Daniel Makinde and L. G. Enyadene, "Modeling heat transfer enhancement of Ferrofluid ($\text{Fe}_3\text{O}_4\text{-H}_2\text{O}$) flow in a microchannel filled with a porous medium," *J Nanofluids*, vol. 10, no. 1, pp. 31–44, 2021. DOI: [10.1166/jon.2021.1764](https://doi.org/10.1166/jon.2021.1764).
- [22] Z. Jibin, Z. Jiming and H. Jianhui, "Design and pressure control of high-pressure differential magnetic fluid seals," *IEEE Trans. Magnetics*, vol. 39, pp. 2651–2653, 2003. DOI: [10.1109/TMAG.2003.815543](https://doi.org/10.1109/TMAG.2003.815543).
- [23] K. Sekine, et al., "Development of a Magnetic fluid shaft seal for an axial-flow blood pump," *Artif Organs*, vol. 27, no. 10, pp. 892–896, 2003. DOI: [10.1046/j.1525-1594.2003.00035.x](https://doi.org/10.1046/j.1525-1594.2003.00035.x).
- [24] H. S. Choi et al., "Simulation of hydrostatical equilibrium of ferrofluid subject to magneto-static field," *IEEE Trans. Magn.*, vol. 44, no. 6, pp. 818–821, 2008. DOI: [10.1109/TMAG.2007.915962](https://doi.org/10.1109/TMAG.2007.915962).

- [25] J. R. Patel and G. Deheri, "Theoretical study of Shliomis model based magnetic squeeze film in rough curved annular plates with assorted porous structures," *FME Trans.*, vol. 42, no. 1, pp. 56–66, 2014. https://www.mas.bg.ac.rs/_media/istrazivanje/fme/vol42/1/08_jpatel.pdf. DOI: 10.5937/fmet1401056P.
- [26] K. Theis-Bröhl, *et al.*, "Self-assembled layering of magnetic nanoparticles in a ferrofluid on silicon surfaces," *ACS Appl Mater Interfaces*, vol. 10, no. 5, pp. 5050–5060, 2018. DOI: 10.1021/acsami.7b14849.
- [27] Y. Amirat and K. Hamdache, "Strong solutions to the equations of a ferrofluid flow model," *J. Math. Anal. Appl.*, vol. 353, no. 1, pp. 271–294, 2009. DOI: 10.1016/j.jmaa.2008.11.084.
- [28] K. Raj, *et al.*, "Advances in ferrofluid technology," *J. Magn. Magn. Mater.*, vol. 149, no. 1-2, pp. 174–180, 1995. DOI: 10.1016/0304-8853(95)00365-7.
- [29] H. Huang, S. Shaheen, K. S. Nisar and M. B. Arain, "Thermal and concentration analysis of two immiscible fluids flowing due to ciliary beating," *Ain Shams Eng. J.*, vol. 15, no. 1, pp. 102278, 2024. DOI: 10.1016/j.asej.2023.102278.
- [30] Y. Li, *et al.*, "Exploring the dynamics of active swimmers microorganisms with electromagnetically conducting stretching through endothermic heat generation/assimilation flow: observational and computational study," *Case Stud. Therm. Eng.*, vol. 51, pp. 103560, 2023. DOI: 10.1016/j.csite.2023.103560.
- [31] N. Fatima, *et al.*, "A case study for heat and mass transfer of viscous fluid flow in double layer due to ciliated channel," *Case Stud. Therm. Eng.*, vol. 45, pp. 102943, 2023. DOI: 10.1016/j.csite.2023.102943.
- [32] M. B. Arain, A. Zeeshan, M. S. Alhodaly, L. Fasheng and M. M. Bhatti, "Bioconvection nanofluid flow through vertical rigid parallel plates with the application of Arrhenius kinetics: a numerical study," *Waves Random and Complex Media*, pp. 1–18, 2022. DOI: 10.1080/17455030.2022.2123115.
- [33] S. U. Rehman, A. Zeeshan, A. Majeed and M. A. Arain, "Impact of Cattaneo-Christov heat flux model on the flow of Maxwell ferromagnetic liquid along a cold flat plate embedded with two equal magnetic dipoles," *JMAG*, vol. 22, no. 3, pp. 472–477, 2017. DOI: 10.4283/JMAG.2017.22.3.472.
- [34] A. Rauf, A. Mushtaq, N. A. Shah and T. Botmart, "Heat transfer and hybrid ferrofluid flow over a nonlinearly stretchable rotating disk under the influence of an alternating magnetic field," *Sci Rep*, vol. 12, no. 1, pp. 17548, 2022. DOI: 10.1038/s41598-022-21784-2.
- [35] S. Zainodin, A. Jamaludin, R. Nazar and I. Pop, "Effects of higher order chemical reaction and slip conditions on mixed convection hybrid ferrofluid flow in a Darcy porous medium," *Alex. Eng. J.*, vol. 68, no. 1, pp. 111–126, 2023. DOI: 10.1016/j.aej.2023.01.011.
- [36] T. Sharma, *et al.*, "Numerical investigation of the hybrid ferrofluid flow in a heterogeneous porous channel with convectively heated and quadratically stretchable walls," *Eur. Phys. J. Plus*, vol. 138, no. 8, pp. 1–8, 2023. DOI: 10.1140/epjp/s13360-023-04371-w.
- [37] W. M. Rosli, M. K. Mohamed, N. M. Sarif, N. F. Mohammad and S. K. Soid, "Boundary layer flow of Williamson hybrid ferrofluid over a permeable stretching sheet with thermal radiation effects," *CFD Letters*, vol. 15, no. 3, pp. 112–22, 2023. DOI: 10.37934/cfdl.15.3.112122.
- [38] S. Idris, A. Jamaludin, R. Nazar and I. Pop, "Heat transfer characteristics of magnetized hybrid ferrofluid flow over a permeable moving surface with viscous dissipation effect," *Heliyon*, vol. 9, no. 5, pp. e15907, 2023. DOI: 10.1016/j.heliyon.2023.e15907.
- [39] H. Zhu, C. Zhang, S. Liu, Y. Tang and Y. Yin, "Effects of nanoparticle clustering and alignment on thermal conductivities of Fe_3O_4 aqueous nanofluids," *Appl. Phys. Lett.*, vol. 89, no. 2, pp. 023123, 2006. DOI: 10.1063/1.2221905.
- [40] R. C. Shah and M. V. Bhat, "Ferrofluid squeeze film in a long journal bearing," *Tribol. Int.*, vol. 37, no. 6, pp. 441–446, 2004. DOI: 10.1016/j.triboint.2003.10.007.
- [41] Q. Raza, X. Wang, B. Ali, M. Z. Qureshi and A. J. Chamkha, "Heat and mass transfer phenomenon and aligned entropy generation with simultaneous effect for magnetized ternary nanoparticles induced by ferro and nano-layer fluid flow of porous disk subject to motile microorganisms," *Numer. Heat Transf. A*, pp. 1–29, 2023. DOI: 10.1080/10407782.2023.2292767.
- [42] Y. M. Chu, *et al.*, "Radiative thermal analysis for four types of hybrid nanoparticles subject to non-uniform heat source: Keller box numerical approach," *Case Stud. Therm. Eng.*, vol. 40, pp. 102474, 2022. DOI: 10.1016/j.csite.
- [43] A. Iqbal and T. Abbas, "A study on heat transfer enhancement of copper (Cu)-ethylene glycol based nanoparticle on radial stretching sheet," *Alex. Eng. J.*, vol. 71, pp. 13–20, 2023. DOI: 10.1016/j.aej.2023.03.025.
- [44] M. N. Sadiq, *et al.*, "Numerical Simulation for flow and heat transfer of a nanofluid over lubricated stretchable surface," *J Nanofluids*, vol. 12, no. 2, pp. 506–513, 2023. DOI: 10.1166/jon.2023.1909.
- [45] S. Maatoug, *et al.*, "A lubricated stagnation point flow of nanofluid with heat and mass transfer phenomenon: significance to hydraulic systems," *J. Indian Chem. Soc.*, vol. 100, no. 1, pp. 100825, 2023. DOI: 10.1016/j.jics.2022.100825.
- [46] H. Yang, *et al.*, "Thermal inspection for viscous dissipation slip flow of hybrid nanofluid ($\text{TiO}_2\text{-Al}_2\text{O}_3/\text{C}_2\text{H}_6\text{O}_2$) using cylinder, platelet and blade shape features," *Sci Rep*, vol. 13, no. 1, pp. 8316, 2023. DOI: 10.1038/s41598-023-34640-8.

- [47] S. A. Alsallami, *et al.*, “Analytical assessment of heat transfer due to Williamson hybrid nanofluid ($\text{MoS}_2 + \text{ZnO}$) with engine oil base material due to stretched sheet,” *Case. Stud. Therm. Eng.*, vol. 51, pp. 103593, 2023. DOI: [10.1016/j.csite.2023.103593](https://doi.org/10.1016/j.csite.2023.103593).
- [48] M. Z. Qureshi, *et al.*, “Thermal performance of hybrid magnetized nanofluids flow subject to joint impact of ferro oxides/CNT nanomaterials with radiative and porous factors,” *Case. Stud. Therm. Eng.*, vol. 41, pp. 102648, 2023. DOI: [10.1016/j.csite.2022.102648](https://doi.org/10.1016/j.csite.2022.102648).
- [49] M. Z. Qureshi, *et al.*, “Heat and mass transfer enhancement of nanofluids flow in the presence of metallic/metallic-oxides spherical nanoparticles,” *Eur. Phys. J. Plus*, vol. 132, no. 1, pp. 1–2, 2017. DOI: [10.1140/epjp/i2017-11342-y](https://doi.org/10.1140/epjp/i2017-11342-y).
- [50] K. Anantha Kumar, N. Sandeep, V. Sugunamma and I. L. Animasaun, “Effect of irregular heat source/sink on the radiative thin film flow of MHD hybrid ferrofluid,” *J Therm Anal Calorim*, vol. 139, no. 3, pp. 2145–2153, 2020. DOI: [10.1007/s10973-019-08628-4](https://doi.org/10.1007/s10973-019-08628-4).
- [51] S. Bilal and M. Z. Qureshi, “Mathematical analysis of hybridized ferromagnetic nanofluid with induction of copper oxide nanoparticles in permeable channel by incorporating Darcy–Forchheimer relation,” *Math Sci*, pp. 1–7, 2021. DOI: [10.1007/s40096-021-00421-5](https://doi.org/10.1007/s40096-021-00421-5).